Protecting Spin Coherence in a Tunable Heisenberg Model: Supplemental Material

(Dated: May 15, 2020)

This supplement provides supporting derivations and details of the experimental methods. In Sec. I, we derive the implemented Hamiltonian and present a simple toy model for the protection of spin coherence. In Sec. II, we elaborate on the experimental sequences and calibrations of atom-cavity coupling and atom number. In Sec. III, we elaborate on the data analysis and modeling.

I. THEORETICAL BACKGROUND

A. Derivation of Tunable Heisenberg Hamiltonian

A theoretical derivation of the cavity-mediated Heisenberg Hamiltonian has been presented in Ref. [1], building on our implementation and analysis for the special case of the XY model in Ref. [2]. Here, we review and expand upon the derivation of the effective spin model

$$H_{\mathrm{XXZ}} = J^{xy}(\Theta)\left(\mathcal{F}_x^2 + \mathcal{F}_y^2\right) + J^z(\Theta)\mathcal{F}_z^2, \tag{S1}$$

where $\boldsymbol{\mathcal{F}}$ is the weighted collective spin defined in the main text. We focus on the relationship of the couplings $J^{xy,z}$ to experimental parameters.

The spin-spin interactions arise from a Faraday interaction between the atoms and the cavity field

$$H_I = \Omega\left(a_+^\dagger a_+ - a_-^\dagger a_-\right)\boldsymbol{\mathcal{F}}\cdot\hat{\mathbf{z}}_{\mathrm{c}}, \tag{S2}$$

where $a_\pm$ represent a pair of circularly polarized cavity modes with respect to the cavity axis $\hat{\mathbf{z}}_{\mathrm{c}}$, and Ω is the average vector ac Stark shift per intracavity photon. Only the spin projection along the cavity axis $\hat{\mathbf{z}}_{\mathrm{c}}$ interacts with the light field. For a cavity driven with linearly polarized light at frequency ω_d, detuned by $\delta = \omega_d - \omega_0$ from cavity resonance, we can expand the atom-cavity interaction Hamiltonian to first order in fluctuations of the vertically polarized cavity mode v to obtain:

$$H_I \approx \frac{\Omega}{\sqrt{(\kappa/2)^2+\delta^2}}\left(\varepsilon e^{-i\delta t}v^\dagger + \mathrm{h.c.}\right)\left[\mathcal{F}_z\cos\Theta + \frac{1}{2}\left(\mathcal{F}_+ e^{i\omega_z t} + \mathcal{F}_- e^{-i\omega_z t}\right)\sin\Theta\right], \tag{S3}$$

where ε parameterizes the drive strength. Provided the occupation of the v mode remains small, we can adiabatically eliminate it from the dynamics to arrive at an effective Hamiltonian for the spins:

$$H_{\mathrm{eff}} = \Omega^2 n\left[\mathcal{F}_z\mathcal{F}_z\ \xi(\delta)\cos^2\Theta + \frac{1}{4}\mathcal{F}_+\mathcal{F}_-\ \xi(\delta_-)\sin^2\Theta + \frac{1}{4}\mathcal{F}_-\mathcal{F}_+\ \xi(\delta_+)\sin^2\Theta\right] \tag{S4}$$

where $n = |\varepsilon|^2/[\delta^2 + (\kappa/2)^2]$ is the average intracavity photon number, $\delta_\pm = \delta \mp \omega_Z$ are the detunings from Raman resonances at $\delta = \pm\omega_Z$, and $\xi(\delta) = \delta/[\delta^2 + (\kappa/2)^2]$.

The effective Hamiltonian H_{eff} in Eq. S4 is related to H_{XXZ} by

$$H_{\mathrm{eff}} = H_{\mathrm{XXZ}} + \frac{1}{4}\Omega^2 n\sum_i c_i^2 f_i^z\left[\xi(\delta_-)) - \xi(\delta_+)\right] \tag{S5}$$

where the second term is negligible for large $\mathcal{F}$ and vanishes in the limit of large detuning $\delta_\pm \gg \omega_Z$. For arbitrary detuning, Eq. S4 shows that the couplings $J^{xy,z}$ take the form

$$J^{xy} = n\Omega^2\mathcal{A}^{x,y}(\Theta,\delta) \tag{S6a}$$

$$J^z = n\Omega^2\mathcal{A}^z(\Theta,\delta). \tag{S6b}$$

Here, the dependence on tuning angle Θ and detuning δ is captured by the functions

$$\mathcal{A}^z(\Theta,\delta) = \xi(\delta)\cos^2\Theta, \tag{S7a}$$

$$\mathcal{A}^{xy}(\Theta,\delta) = \frac{\sin^2\Theta}{4}\left[\xi(\delta_-) + \xi(\delta_+)\right]. \tag{S7b}$$

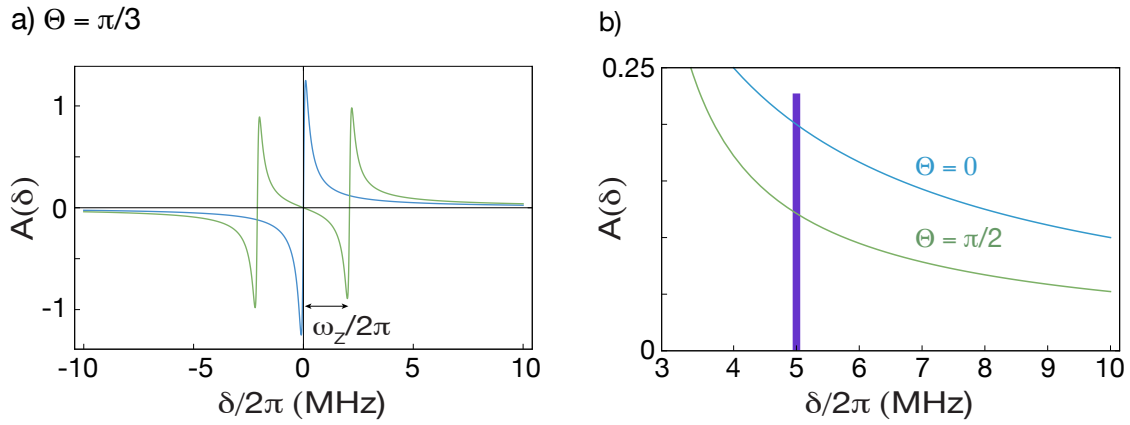

FIG. S1: Dependence of interactions on detuning for $(\kappa, \omega_Z) = 2\pi \times (0.2, 2.1)$ MHz. (a) The functions $\mathcal{A}^{xy}(\Theta = \pi/3, \delta)$ (green) and $\mathcal{A}^{z}(\Theta = \pi/3, \delta)$ (blue) are plotted here at fixed Θ to show that all four relative signs of XY and Ising couplings are accessible. (b) We zoom in on the functions $\mathcal{A}^{xy}(\Theta = \pi/2, \delta)$ (green) and $\mathcal{A}^{z}(\Theta = 0, \delta)$ (blue), which determine the strengths of XY and Ising couplings, at larger detuning. In the large detuning limit, $\mathcal{A}^{z}(0, \delta)/\mathcal{A}^{xy}(\pi/2, \delta) = 2$. Our drive field (purple) is typically placed around $\delta/2\pi \sim 5$ MHz, where this ratio is 1.6.

They are plotted for $\Theta = \pi/3$ in Fig. S1a, illustrating that all four relative signs $(++), (--), (+-), (-+)$ of the Ising and XY couplings are achievable by adjusting the drive detuning. The couplings at large detuning $\delta \gg \kappa, \omega_Z$ compared to the cavity linewidth κ and Zeeman splitting ω_Z are plotted in Fig. S1b. In this regime, Eq. S5 simplifies to

$$H_{\text{eff}} = \frac{n\Omega^2}{\delta}\left[\cos^2\Theta \mathcal{F}_z^2 + \frac{1}{2}\sin^2\Theta\left(\mathcal{F}_x^2 + \mathcal{F}_y^2\right)\right], \tag{S8}$$

and $J_z(0)/J^{xy}(\pi/2) = 2$. For the drive detunings $\delta \approx 2\pi \times 5$ MHz used for the measurements in Fig. 2c of the main text, we expect a ratio of 1.6, consistent with the displayed fits.

B. Model for Dephasing

Here we present an estimate of the critical interaction strength for protecting spin coherence in a simplified system. We consider a collection of atoms in which the only source of inhomogeneity is a field along $\hat{\mathbf{z}}$ that takes on values $+h_z\hat{\mathbf{z}}$ and $-h_z\hat{\mathbf{z}}$ in two different regions of the cloud. We assume that the collective spin vectors $\mathbf{S}_1$ and $\mathbf{S}_2$ in these two regions are both initially polarized along $\hat{\mathbf{x}}$ and analyze their response to the inhomogeneous field. The total Hamiltonian is

$$H_{\text{XXZ}}/\hbar + H_{\text{inh}}/\hbar = J^{xy}(\Theta)\left[F_x^2 + F_y^2\right] + J^z(\Theta)F_z^2 + \sum_i h_{i,z}S_{i,z}, \tag{S9}$$

where $\mathbf{F} = \sum_i \mathbf{S}_i$ is the equally weighted sum of the two collective spin vectors. F_z commutes with the Hamiltonian and is thus conserved. The system is also invariant under exchange of the two spins followed by a 180 degree rotation about $\hat{\mathbf{x}}$. Due to this symmetry, we can describe the whole system with the three components (S_x, S_y, S_z) of a single collective spin. Ignoring quantum fluctuations, the other spin has components $(S_x, -S_y, -S_z)$ and the total spin is $\mathbf{F} = (2S_x, 0, 0)$.

The dynamics of the spin $\mathbf{S}$ are constrained by two more conserved quantities: the length of each collective spin and the total energy of the system. The equation for each collective spin, $S^2 = S_x^2 + S_y^2 + S_z^2 = \text{const}$, maps out the surface of a Bloch sphere. The total energy is given by the Hamilitonian, which using the classical expression for the total spin reduces to $4J^{xy}(\Theta)S_x^2 + 2h_zS_z = E$.

We plot projections of constant energy contours on the surface of the Bloch sphere in the equatorial plane in Fig. S2. These contours are qualitatively different for values of J^{xy} above and below the critical point in this model, $J_c^{xy} = 2h_z/S$. When $SJ^{xy} < 2h_z$, the contours encircle the north pole of the Bloch sphere, permitting dephasing. For larger values of $J^{xy}(\Theta)$, the contours break into two disjoint cycles and the two collective spins remain localized,

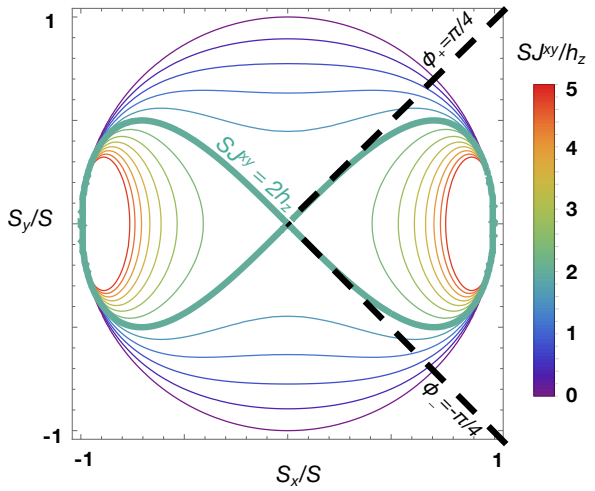

FIG. S2: **Toy model for critical interaction strength.** Contours of constant energy are sketched on the Bloch sphere as viewed from the north pole, for spins initially aligned with $\hat{\mathbf{x}}$. The critical interaction strength (thick green curve) is labeled. Above this critical strength, the phase evolution of a single spin ($\mathbf{S}_1$ or $\mathbf{S}_2$) along a constant-energy contour remains between $\phi_\pm = \pm\pi/4$, bounding the angle between spins $\mathbf{S}_1$ and $\mathbf{S}_2$ to be at most $\phi_+ - \phi_- = \pi/2$.

.

bounding the phase accumulation between them. This approach agrees with the scaling of the estimate based on the energy gap.

II. EXPERIMENTAL METHODS

A. Preparation and Detection

The atoms are cooled and trapped in a magneto-optical trap in the center of the cavity, and then loaded into the trapping lattice after an optical molasses cooling stage. In lieu of optical pumping, atoms not in $|f = 1, m_f = -1\rangle$ are removed by adiabatically sweeping $m_f = 0, 1$ atoms into the $f = 2$ manifold, then pushing them out of the trap with resonant light on the $\left|5S_{1/2}, f = 2\right\rangle \rightarrow \left|5P_{3/2}, f' = 3\right\rangle$ transition. We thus obtain a spin-polarized state in $|f = 1, m_f = -1\rangle$, which forms the starting point for preparing any desired spin texture using the focused scanning Raman beam (Fig. S3). After state preparation, the magnetic field is tuned to the angle Θ, and the drive laser is then switched on to generate interactions. Throughout the interaction time, the trap depth is $h \times 5$ MHz corresponding to a transverse trap frequency of 1.5 kHz.

We perform state detection by measuring the three spin components $(\langle f_x\rangle, \langle f_y\rangle, \langle f_z\rangle)$ in three separate runs of the experiment. In order to measure the magnetization $\langle f_z\rangle \equiv \rho_1 - \rho_{-1}$, where ρ_k is the local atomic density in the $m_f = k$ Zeeman level, we perform state-sensitive imaging in each of the three Zeeman levels $m_f = \pm 1, 0$. Sequentially, we transfer each m_f population into $f = 2$ with an adiabatic microwave sweep and perform fluorescence imaging on the $\left|5S_{1/2}, f = 2\right\rangle \rightarrow \left|5P_{3/2}, f' = 3\right\rangle$ transition, simultaneously lowering the trap so the imaged atoms are kicked out of the trap by the imaging light. In order to measure the transverse spin components $\langle f_x\rangle$ or $\langle f_y\rangle$, we image after an additional global Raman $\pi/2$ pulse with phase 0 or $\pi/2$, respectively, to rotate the transverse spin component into the z-basis.

We calibrate our imaging pulses by measuring Rabi oscillations induced by a global Raman beam. The distribution of atoms in the three m_f levels during these oscillations reveals systematic errors including atom loss on each imaging pulse and imperfect removal of previously imaged states, as well as residual atoms initially in $m_f \neq -1$. To characterize these errors, we optimize a 3×3 matrix M to minimize $\sum_t (M\boldsymbol{\rho}^{\text{meas}}(t) - \boldsymbol{\rho}^{\text{theory}}(t))^2$. Here, $\boldsymbol{\rho}$ is a vector specifying the populations in the three Zeeman states and $\boldsymbol{\rho}^{\text{theory}}$ describes Rabi oscillations of full contrast, as justified by the measured Rabi coherence time. Assuming that the imperfections in imaging and state preparation are constant for a given data run, we then apply M on all measured data to accurately determine the magnetization.

B. Atom-Cavity Coupling

Here we derive the dimensionless weights $c(\zeta)$ parameterizing the spatial dependence of the Faraday coupling of atoms to the cavity mode. These weights depend both on the position $\zeta = z_c/z_R$ at which the atoms are pinned by the 1560 lattice and on the temperature, which determines the radial and axial distributions of atoms within each lattice site.

As a function of distance from cavity center z_c and radial distance r from the optical axis, the intensity profiles (neglecting wavefront curvature) for the two modes are given by

$$I/I_{\max} = (w_0/w)^2 e^{-2r^2/w^2} \cos^2(kz_c - \psi), \tag{S10}$$

where $\psi(\zeta) = \tan^{-1}(\zeta)$ is the Gouy phase shift and $w(\zeta) = w_0\sqrt{1+\zeta^2}$ is the waist. The Rayleigh range $z_R = 1.4$ mm is determined by the cavity geometry and is the same for both lattices. The wavenumbers and waists for the two lattices are related by $k_{780} = 2k_{1560}$ and $w_{780}(\zeta) = w_{1560}(\zeta)/\sqrt{2}$.

Atoms imaged at position ζ are trapped around the nearest antinode of the 1560 nm lattice, $z_{peak} = (n\pi + \psi(\zeta))/k_{1560}$. Approximating the trap potential as harmonic near the antinode, the thermal distribution of atoms is

$$P(\Delta z, r) \propto e^{-(k_{1560}\Delta z)^2/\tau} e^{-2(r/w_{1560})^2/\tau}, \tag{S11}$$

where $\Delta z \equiv z_c - z_{peak}$ and τ is the temperature normalized to trap depth at a given position ζ. For the same trapping site at position ζ, the intensity of the 780 nm drive mode is

$$I_{780}(\Delta z, r) = \frac{I_{\max}}{1+\zeta^2} e^{-2r^2/w_{780}^2} \cos^2(k_{780}\Delta z + \psi(\zeta)). \tag{S12}$$

We compute the couplings $c(\zeta)$, normalized to the coupling $c_{\max}$ of an atom at cavity center ($z_c = r = 0$), by averaging the intensity of the light field over the distribution of atoms,

$$\frac{c(\zeta)}{c_{\max}} = \frac{\int I_{780}(\Delta z, r) P(\Delta z, r) d^3r}{\int I_{\max} P(\Delta z, r) d^3r} = \frac{1}{1+2\tau}\left[\frac{e^{-4\tau}}{(1+\zeta^2)^2} + \frac{1}{2}\frac{1-e^{-4\tau}}{1+\zeta^2}\right]. \tag{S13}$$

The factor $1/(1+2\tau)$ comes from comparing the radial distribution to the waist of the drive mode while $e^{-4\tau}$ compares the width of the axial distribution to the lattice spacing. When atoms are warm, they experience an averaged probe coupling that decays as w^{-2}. When the atoms are cold, coupling to the drive mode at cavity center is higher, but the offset between the maxima of the trapping lattice and the maxima of the drive mode (due to the Gouy phase shift) causes coupling to decay more quickly as w^{-4}.

The functional form of the couplings in Eq. S13 is corroborated by spectroscopic measurements of the vector light shift, similar to the measurement described in Ref. [2]. Fitting the spatial dependence of the vector light shift yields a temperature parameter $\tau = 0.3(1)$. When the couplings are normalized such that their average value is 1, the maximum coupling becomes $c_{\max} = \Omega_0/\Omega$. We compute Ω_0 from g as in the main text. For a maximally coupled atom at cavity center, $g^2 = 6\Gamma\omega_{\mathrm{FSR}}/(\pi k_{780}^2 w_0^2)$ where $\Gamma = 2\pi \times 6.07$ MHz is the linewidth of the transition and $\omega_{\mathrm{FSR}} = 2\pi \times 3.0$ GHz is the free spectral range of the cavity [3]. The waist of the 780 nm mode is $w_0 = 18.6$ μm, calculated from the measured transverse mode spacing. These values yield $2g = 2\pi \times 2.5$ MHz corresponding to $\Omega_0 = 2\pi \times 23$ Hz. We then determine Ω using Eq. S13 with our measured value for τ.

C. Cavity Shift and Atom Number

We calibrate the atom number by measuring the dispersive shift of the cavity resonance frequency, which is proportional to the total weighted atom number N. In particular, in addition to the Faraday interaction that generates birefringence proportional to $\mathcal{F}_z$, the Hamiltonian includes a term

$$H_s = 4\Omega N\left(a_+^\dagger a_+ + a_-^\dagger a_-\right). \tag{S14}$$

This term describes a common-mode shift of the σ_+ and σ_- cavity resonances that depends on the number of coupled atoms

$$\Delta\omega \equiv \omega_0(N) - \omega_0(0) = -4\Omega N. \tag{S15}$$

In the main text, we let $\omega_0 \equiv \omega_0(N)$ represent the atom-shifted cavity resonance frequency for total weighted atom number N. For the measurements in the main text, we typically measure $\Delta\omega \approx -2\pi \times 2.5$ MHz. In combination with our determination of the average single-photon vector light shift Ω (Sec. II B), we use $\Delta\omega$ to calibrate the total atom number, and to calibrate the number of counts per atom obtained in images of the magnetization.

D. Experimental Sequences

In this section, we give further details describing the experimental sequences used throughout the main text. In particular, we give numerical values for relevant experimental parameters and provide qualitative illustrations of the pulse sequences and time-changing parameters for conceptual clarity.

Hamiltonian tomography. The sequences used for Hamiltonian tomography as shown in Fig. 2 of the main text are illustrated in Fig. S3. These measurements were performed in a 3 G field. To measure the Ising coupling or XY couplings, the state $|\psi_z\rangle$ or $|\psi_y\rangle$ is prepared via both local and global Raman rotations. The weighted probe spins in regions B and C point in opposite directions and are equal in length to within 5% of the total weighted spin vector. After preparation of the target initial state, the drive laser is then switched on for t_{int} to generate interactions. A final global $\pi/2$ pulse with phase $\varphi = 0$ ($\pi/2$) then rotates the desired quadrature x (y) into the population basis, whence it is measured with the detection sequence described in Sec. II A. Alternatively, $\langle f_z \rangle$ can be measured directly without the extra $\pi/2$ rotation.

For measurements of the Ising coupling, an optional spin echo may be performed by adding a global π pulse halfway through the interaction time (Fig. S3a). The spin echo ensures that the measured spin precession is solely due to interactions, and would cancel the effect of any circular polarization of the intracavity light that is independent of the atomic magnetization. In the main text, all measurements of $J^{xy,z}(\Theta)$ in Fig. 2(c) were performed with spin echo, and are consistent with the measurement in Fig. 2(a) that is performed without spin echo.

The location of the atom cloud shifted between measurements of the XY and Ising couplings, resulting in slightly different optimal choices for the regions A, B, C.

Magnetic susceptibility. The sequence for measuring susceptibility as in Fig. 3 of the main text is illustrated in Fig. S4a. We prepare the ground state of an effective field $H_0 = h_x F_x + h_z F_z$. The interactions are then ramped on, thus preparing a low-energy state of $H_{\mathrm{tot}} = H_{\mathrm{XXZ}} + H_0$ (but not the quantum ground state). Finally, the effective field and interactions are simultaneously quenched off and $\langle f_z \rangle$ is measured immediately. These measurements were performed in magnetic fields ranging between 1 and 3 G.

Dephasing and gap protection. The sequence for measuring dephasing as in Fig. 4 of the main text is illustrated in Fig. S4b. We prepare the ground state of $H_0 = h_x F_x + \sum_i h_{i,z} f_{i,z}$, where $h_{i,z}$ varies linearly across the cloud as $h_z(\zeta) = \mu\zeta$. The interactions are then ramped on, and the spins evolve under $H_{\mathrm{XXZ}} + \sum_i h_{i,z} f_{i,z}$ for a time $0 \leq t_{\mathrm{wait}} \leq 1$ ms before the measurement of $\langle f_x \rangle, \langle f_y \rangle, \langle f_z \rangle$. These measurements were performed in a 1 G field.

Experimental timescales. In each of the measurement sequences described above, the choice of overall timescale for the experiment is governed by technical considerations. The timescale for the experiments in Fig. 2 is lower-bounded by our timing resolution and the cavity lifetime, i.e. we cannot resolve time steps smaller than a few microseconds. The experiment length is upper-bounded by several factors, including inhomogeneous broadening due to a residual external magnetic field gradient and transverse atomic motion. We chose the timescale for the data in Fig. 2 to lie between these two limits. In Figs. 3 and 4, the timescale is somewhat longer and lower-bounded by the Rabi frequency of the Raman coupling and the magnetic field gradient.

III. ANALYSIS AND MODELING

A. Mean-Field Simulations of Dynamics under H_{XXZ}

To verify our understanding of the dynamics used for Hamiltonian tomography, we simulate the evolution under H_{XXZ} in a mean-field approximation. The mean-field dynamics are obtained by computing the Heisenberg equations of motion $dO/dt = i[H, O]$ and substituting $O \to \langle O \rangle$, thus ignoring all higher-order correlations. Concretely, we numerically simulate a system with β spatial modes along the cavity axis by solving 3β coupled differential equations

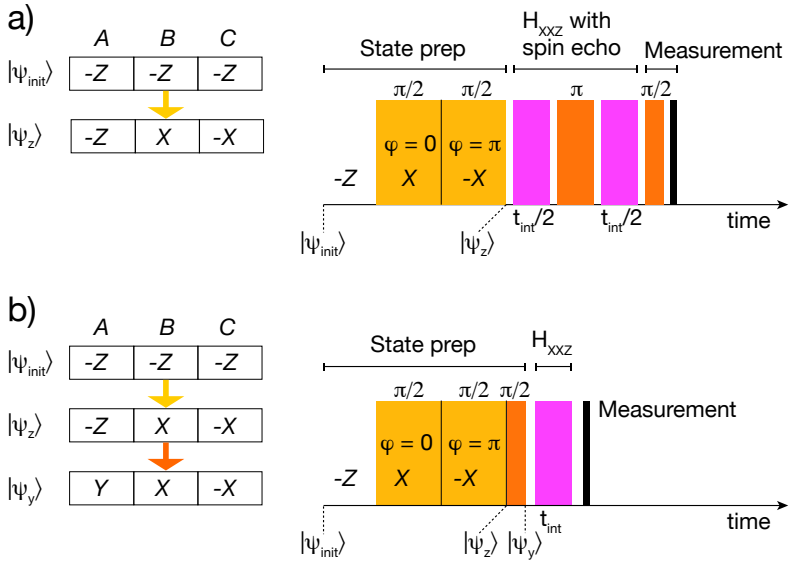

FIG. S3: Sequences for measuring Ising and XY Couplings. (a) To measure the Ising coupling, $|\psi_z\rangle$ is prepared by scanning a focused Raman beam of variable amplitude and phase (yellow) across the cloud. Locally, it performs a $\pi/2$ rotation with the desired phase such that the spins point along $\hat{\mathbf{x}}$ ($\varphi = 0$) or $-\hat{\mathbf{x}}$ ($\varphi = \pi$) in regions B and C. To leave the atoms in region A pointing down along $-\hat{\mathbf{z}}$, the Raman amplitude is locally set to zero. The drive laser is then switched on for a time $t_{\rm int}$ (pink) to generate interactions. The optional spin echo consists of a π pulse applied with a global Raman beam (orange) in the middle of $t_{\rm int}$. A final global $\pi/2$ pulse (orange) then rotates the desired quadrature x (y) into the population basis and the $m_f = \pm 1, 0$ populations are measured (black). (b) To measure the XY coupling, the state $|\psi_y\rangle$ is prepared by making $|\psi_z\rangle$ as in (a). The $-\hat{\mathbf{z}}$ spins are then rotated by a global $\pi/2$ pulse about $-\hat{\mathbf{x}}$ (orange) to point along $-\hat{\mathbf{y}}$. The drive laser is switched on for time $t_{\rm int}$, after which the populations in $m_f = \pm 1, 0$ are measured (black).

for $(\langle f_x\rangle, \langle f_y\rangle, \langle f_z\rangle)$:

$$\frac{d\langle f_x(t,\zeta)\rangle}{dt} = -2c(\zeta)\left[J^z\mathcal{F}_z(t)\langle f_y(t,\zeta)\rangle - J^{xy}\mathcal{F}_y(t)\langle f_z(t,\zeta)\rangle\right] \tag{S16a}$$

$$\frac{d\langle f_y(t,\zeta)\rangle}{dt} = 2c(\zeta)\left[J^z\mathcal{F}_z(t)\langle f_x(t,\zeta)\rangle - J^{xy}\mathcal{F}_x(t)\langle f_z(t,\zeta)\rangle\right] \tag{S16b}$$

$$\frac{d\langle f_z(t,\zeta)\rangle}{dt} = -2J^{xy}c(\zeta)\left[\mathcal{F}_y(t)\langle f_x(t,\zeta)\rangle - \mathcal{F}_x(t)\langle f_y(t,\zeta)\rangle\right] \tag{S16c}$$

After plugging in measured values for the relevant quantities $\Omega, c(\zeta), \Delta\omega, \delta, \Theta$, we obtain the dynamics plotted in Fig. S5. These simulated dynamics, with the intracavity photon number n as the only free parameter, are in good agreement with the experimental data in Fig. 2 of the main text. Similar equations are used to generate the mean-field model curves in Fig. 4d of the main text.

B. Model for Susceptibility

We compare the measured magnetic susceptibility in Fig. 3 of the main text with a mean-field model, in which we approximate the collective spin vectors $\boldsymbol{\mathcal{F}}$ and $\mathbf{F}$ by their expectation values. Since the system is initialized in a spin-polarized state, the weighted and unweighted collective spins initially have the same orientation $\boldsymbol{\mathcal{F}} \parallel \mathbf{F}$. Assuming that this condition remains true throughout the susceptibility measurement, the XXZ Hamiltonian with additional effective fields

$$H_{\rm tot} = J^z_{\rm eff}\mathcal{F}_z^2 + h_x F_x + h_z F_z \tag{S17}$$

can be expressed in terms of the angle $\alpha \equiv \arctan(F_z/F_x)$ of the Bloch vector from the $\hat{\mathbf{x}}$-axis as

$$H_{\rm tot} = J^z_{\rm eff}\mathcal{F}^2\sin^2\alpha + h_x F\cos\alpha + h_z F\sin\alpha. \tag{S18}$$

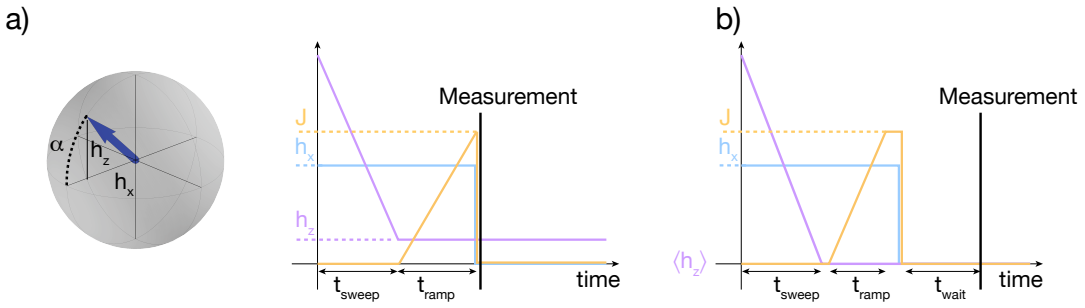

FIG. S4: Sequences for susceptibility and dephasing measurements. (a) To measure the magnetic susceptibility, we sweep the Raman detuning (purple) over a time $t_{\rm sweep} = 5$ ms from far off-resonance to a final value h_z. At fixed Rabi frequency h_x (blue), the angle $\alpha = \arctan(h_z/h_x)$ of the collective spin vector on the Bloch sphere, measured from the $\hat{\mathbf{x}}$-axis, is thus determined. The interactions (yellow) are then ramped on over a time $t_{\rm ramp} = 5$ ms to a final value J, after which the effective field and interactions are simultaneously quenched off and the magnetization is measured immediately. (b) To measure the dephasing in a magnetic field gradient, the average Raman detuning (purple) is swept during $t_{\rm sweep} = 5$ ms from far off-resonance to zero, such that the collective spin vector points on average along $\hat{\mathbf{x}}$. Interactions are then ramped on to a final value J during $t_{\rm ramp} = 5$ ms. The spins evolve under $H_{\rm XXZ} + H_{\rm inh}$ for a time $0 \le t_{\rm wait} \le 1$ ms before the measurement is performed.

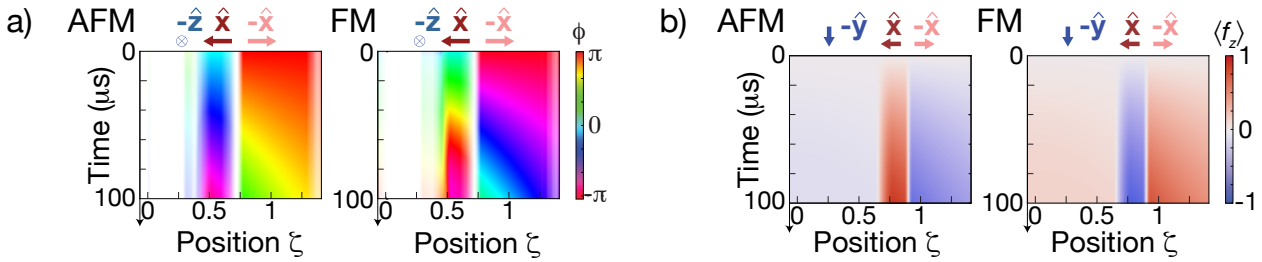

FIG. S5: Mean-field simulations corresponding to Fig. 2 of the main text for (a) Ising and (b) XY couplings. With $\Theta \approx 53°$, we plot (a) phase ϕ, with opacity indicating transverse spin length, or (b) magnetization $\langle f_z \rangle$. We compare both signs of drive detuning δ to check the agreement for antiferromagnetic (AFM) [(a) $\delta = 2\pi \times 7.5$ MHz, (b) $2\pi \times 5.5$ MHz] and ferromagnetic (FM) [(a) $\delta = -2\pi \times 5.5$ MHz (b) $-2\pi \times 5.5$ MHz] couplings. The intracavity photon number varies from $n \approx 5000$ in (b) to $n \approx 15000$ in (a) AFM and 20000 in (a) FM, which agrees within uncertainty with the measured intracavity photon number for these data.

To find the minimum energy configuration for the angle α as a function of the parameters h_x, h_z, we solve

$$\frac{\partial H_{\rm tot}}{\partial \alpha} = 2J^z_{\rm eff}\mathcal{F}^2 \sin\alpha\cos\alpha - h_x F \sin\alpha + h_z F \cos\alpha = 0. \tag{S19}$$

Taking the derivative of Eq. S19 with respect to h_z, we solve for the susceptibility, with $\alpha(h_z = 0) = 0$:

$$\chi \equiv \left.\frac{\partial \sin\alpha}{\partial(h_z/h_x)}\right|_{h_z=0} = \frac{\cos^2\alpha}{2J^z_{\rm eff}\mathcal{F}^2(2\cos^2\alpha - 1)/h_x F + \cos\alpha} = \frac{1}{2J^z_{\rm eff}\mathcal{F}^2/h_x F + 1} \tag{S20}$$

$$= \frac{1}{2\Lambda^z_{\rm eff}/h_x + 1}, \tag{S21}$$

Note that in the main text we equivalently define the susceptibility in terms of the polar angle $\theta = \pi/2 - \alpha$.

Equation S21 shows that the susceptibility diverges at a critical value $\Lambda^z_{\rm eff} = -h_x/2$ of the collective interaction parameter. The physical meaning of the diverging susceptibility at the critical point can be understood by examining the energy landscape (Eq. S19) above and below the critical interaction strength, as sketched in Fig. S6. For no interactions, the minimum energy shifts smoothly as a function of h_z, but at the critical point the parabolic landscape

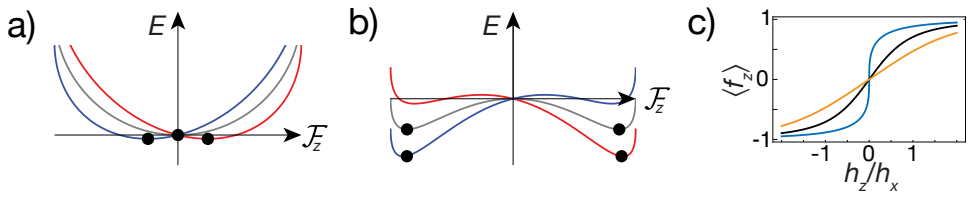

FIG. S6: (a-b) Energy landscape of transverse-field Ising model in the classical limit for three different values of h_z: $h_z < 0$ (red), $h_z > 0$ (blue), and $h_z = 0$ (gray). The energy minimum for the non-interacting model (a) varies smoothly with varying h_z. With ferromagnetic Ising interactions (b), the energy minimum instead jumps discontinuously between the two local minima of a tilted double-well potential. (c) Sample curves of the magnetic susceptibility as a function of h_z/h_x, plotted for $\Lambda^z_{\text{eff}}/h_x = -0.5$ (blue), $\Lambda^z_{\text{eff}}/h_x = 0$ (black), and $\Lambda^z_{\text{eff}}/h_x = 0.5$ (orange).

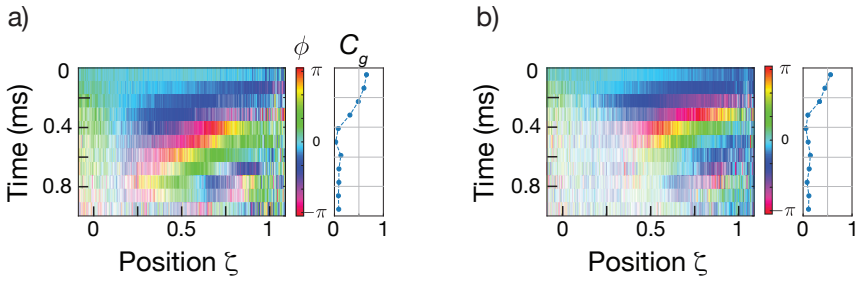

FIG. S7: (a-b) Phase ϕ and global contrast C_g at $\Theta = 0$ for (a) no interactions and (b) Ising interactions [$J^z\mathcal{F}/\mu L = 0.52(5)$], in magnetic field gradient $|\mu| = 2\pi \times 2$ kHz$/L$. Opacity indicates length of transverse spin component.

becomes a tilted double well potential, whose minimum jumps between two separate wells as h_z is tuned through zero.

We use the model in Eq. S21 to fit the susceptibility measurements in Fig. 3(c) of the main text. There, the susceptibility χ is determined from measurements of the magnetization $\langle f_z \rangle$ as a function of h_z/h_x. Specifically, we fit the magnetization data using the the model in Eq. S19 for the angle α as a function of $J^z_{\text{eff}}, h_x, h_z$, which can in general be solved numerically to yield curves of the form shown in Fig. S6(c). We calibrate h_x using a fit to the magnetization of the non-interacting system, where $\alpha = \arctan(h_z/h_x)$ [Fig. 3(b.i) of main text]. We then fit Eq. S19 numerically to the data with interactions, such as those shown in Fig. 3(b.ii-iii) of the main text, and determine the magnetic susceptibility χ from the slope of each fitted curve at $h_z = 0$. The results are plotted in Figs. 3c and 3d of the main text, showing χ as a function of $\Lambda^{xy,z}$ and of Θ.

C. Dephasing Analysis

In addition to the measurements at $\Theta = \pi/2$ shown in Fig. 4(a-b) of the main text, we also measure dephasing at $\Theta = 0$ with and without Ising interactions, as plotted in Fig. S7. We use the data with no interactions to calibrate the gradient across a region of length $L = 1$ mm by performing a linear fit to the phase $\phi_L(t)$. In Fig. 4c of the main text, we plot this fit line together with the phase $\phi_L(t)$ extracted from the data with Ising interactions.

[1] G. Bentsen, I.-D. Potirniche, V. B. Bulchandani, T. Scaffidi, X. Cao, X.-L. Qi, M. Schleier-Smith, and E. Altman, Phys. Rev. X **9**, 041011 (2019), URL `https://link.aps.org/doi/10.1103/PhysRevX.9.041011`.

[2] E. J. Davis, G. Bentsen, L. Homeier, T. Li, and M. H. Schleier-Smith, Phys. Rev. Lett. **122**, 010405 (2019), also see Supplemental Material., URL `https://link.aps.org/doi/10.1103/PhysRevLett.122.010405`.

[3] H. Tanji-Suzuki, I. D. Leroux, M. H. Schleier-Smith, M. Cetina, A. T. Grier, J. Simon, and V. Vuletić, in Advances in atomic, molecular, and optical physics (Elsevier, 2011), vol. 60, pp. 201–237.